



# **JGR** Planets

### **RESEARCH ARTICLE**

10.1029/2024JE008296

#### **Key Points:**

- We measured the strength and stiffness of LL6 chondritic materials under conditions relevant to the rocky interiors of small icy moons
- The relationship between confining pressure, stiffness, and strength of LL6 chondritic material changes at 40– 50 MPa confining pressure
- Pressurization and deformation of LL6 chondritic material dissipate energy in response to small stress changes

#### **Supporting Information:**

Supporting Information may be found in the online version of this article.

#### Correspondence to:

C. Seltzer, cseltz@mit.edu

#### Citation:

Seltzer, C., O'Ghaffari, H., & Peč, M. (2024). Mechanical properties of LL6 chondrites under pressures relevant to rocky interiors of icy moons. *Journal of Geophysical Research: Planets*, 129, e2024JE008296. https://doi.org/10.1029/2024JE008296

Received 16 JAN 2024 Accepted 19 JUN 2024

# © 2024. The Author(s). This is an open access article under the terms of the Creative Commons Attribution License, which permits use, distribution and reproduction in any medium, provided the original work is properly cited.

# **Mechanical Properties of LL6 Chondrites Under Pressures Relevant to Rocky Interiors of Icy Moons**

Cassandra Seltzer<sup>1</sup>, Hoagy O'Ghaffari<sup>1</sup>, and Matěj Peč<sup>1</sup>

<sup>1</sup>Department of Earth, Atmospheric, and Planetary Sciences, Massachusetts Institute of Technology, Cambridge, MA, USA

**Abstract** Icy moons in the outer Solar System likely contain rocky, chondritic interiors, but this material is rarely studied under confining pressure. The contribution of rocky interiors to deformation and heat generation is therefore poorly constrained. We deformed LL6 chondrites at confining pressures  $\leq 100$  MPa and quasistatic strain rates. We defined a failure envelope, recorded acoustic emissions (AEs), measured ultrasonic velocities, and retrieved static and dynamic elastic moduli for the experimental conditions. The Young's modulus, which quantifies stiffness, of the chondritic material increased with increasing confining pressure. The material reached its peak strength, which is the maximum supported differential stress ( $\sigma_1 - \sigma_3$ ), between 40 and 50 MPa confining pressure. Above this 40–50 MPa range of confining pressure, the stiffness increased significantly, while the peak strength dropped. Acoustic emission events associated with brittle deformation mechanisms occurred both during isotropic pressurization ( $\sigma_1 = \sigma_2 = \sigma_3$ ) as well as at low differential stresses during triaxial deformation ( $\sigma_1 > \sigma_2 = \sigma_3$ ), during nominally "elastic" deformation, indicating that dissipative processes are likely possible in the rocky interiors of icy moons. These events also occurred less frequently at higher confining pressures. We therefore suggest that the chondritic interiors of icy moons could become less compliant, and possibly less dissipative, as a function of the moons' pressure and size.

Plain Language Summary Many icy moons in the outer Solar System have warm, active interiors, but it is difficult to estimate heat generation in the smallest icy moons. As moons orbit their host planets, forces and stresses can cause moon material to change shape, or deform; this process releases heat. The deformation expected in the outermost layers is not always sufficient to explain heat fluxes in small moons, so we conducted a comprehensive experimental study of the properties of rocky material comprising the innermost layers. As this material is thought to be similar in composition to meteorites, we experimentally deformed meteoritic samples at elevated confining pressures similar to those inside of small icy moons. We observed acoustic energy emission associated with deformation at all stages of pressurization, and particularly in response to small changes in stress. We also found that the material behaved differently at low and high confining pressures. These observations indicate that icy moons with smaller oceans and thinner crusts with cores of similar composition to our samples may have interiors that deform differently than those of larger icy moons, and thus might receive some of the heat needed to maintain their oceans through deformation processes in their porous cores.

# 1. Introduction

Icy moons in the outer Solar System are considered excellent candidate bodies for hosting extraterrestrial life. The interior properties of these moons are important for determining the feasibility of life, lander missions, and future priorities in exploring the outer Solar System. The mechanical properties of the cores of these moons are relatively less well-studied than the properties of their icy crusts and water oceans, as the cores are likely less dissipative than the ice or liquid layers (e.g., Tobie et al., 2005). The deformation mechanisms of core material are thus presently still poorly constrained, leaving large uncertainties as to how dissipation proceeds throughout the entire body: there is an order-of-magnitude difference in potential heat release from Enceladus' core, for example, depending on whether it is stiff and elastic or if it is highly deformable and (poro)viscoelastic (Aygün & Čadek, 2022; Rovira-Navarro et al., 2022).

The yield strength and elastic moduli of a material, which can be used to predict how a body responds to stress, are almost always pressure- and strain-rate dependent (Mair et al., 2002; Mulliken & Boyce, 2006). Rocky components of icy moons are frequently thought to be chondritic in nature (Kuskov & Kronrod, 2005; Néri et al., 2020; Neumann & Kruse, 2019), yet most strength tests of meteoritic material are conducted at asteroidal conditions: no confinement, and fast strain rates (see Pohl & Britt, 2020 for a review).

SELTZER ET AL. 1 of 11

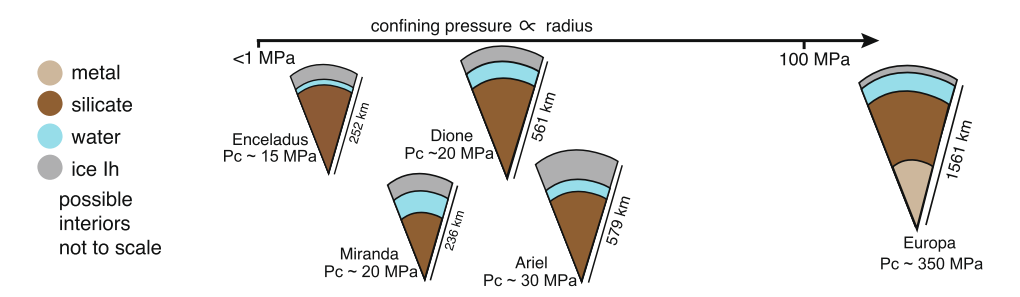


Figure 1. Sample interior models for small icy moons, shown in order of increasing confining pressure, *Pc*, at the ocean-rock interface, based on estimates from PlanetProfile by Vance et al. (2018) and Styczinski et al. (2023).

Confining pressures at the core-ocean or core-mantle boundary of icy moons can reach tens of MPa and more (Figure 1; Neveu et al., 2015; Styczinski et al., 2023; Vance et al., 2018). However, almost all tests on meteoritic material occur at room pressure (Pohl & Britt, 2020). The few tests that assess the strength and deformation mechanisms of chondritic material under pressure (Ramesh et al., 2017; Voropaev et al., 2017) do not report strength at pressures relevant to rocky interiors of icy moons. Voropaev et al. (2020) studied a single sample at a confining pressure of 50 MPa, but did not apply any differential stress and therefore could not measure the strength or stiffness of the material at this pressure range. Dynamic (fast) deformation experiments simulating crater formation and impacts on chondrites are also common. These experiments are not easily applied to planetary deformation at lower strain rates, and there is a larger rate sensitivity in unconfined meteoritic material than in terrestrial rocks (Kimberley & Ramesh, 2011). Hogan et al. (2015) used Brazilian disk tests in a Kolsky bar apparatus under confined planar configuration at dynamic strain rates of  $10^1-10^3$  s<sup>-1</sup>, which yielded a higher peak strength (~300 MPa) than the unconfined tests at similar strain rates, but did not record enough data at low strain rates to establish a definite change in peak strength for quasistatic tests conducted at no confining pressure versus those conducted under confinement.

Here, we report the mechanical properties of deforming chondritic material under elevated confining pressure. These measurements represent the first experimental investigation of chondritic material deformation under confining pressure similar to that found inside an icy moon. We used fallen meteoritic material, which is inherently pre-deformed and high-strength. These fallen meteorites are potential analogs for the rocky cores and mantles of moons, which have likely survived continuous tidal deformation over billions of years (Nimmo & Pappalardo, 2016).

In addition to the bulk mechanical response to deformation, we also used ultrasound probes to study the dynamic behavior as the rocks were pressurized and subsequently deformed. Brittle deformation that causes damage to the material can emit dynamic stress waves, observable as acoustic emissions (AEs) with characteristic frequencies depending on the source characteristics (Eitzen & Wadley, 1984; Ghaffari et al., 2014; Lei & Ma, 2014; Li et al., 2021; O'Ghaffari et al., 2023). These deformation mechanisms include microcracking and frictional sliding along new surfaces, both of which dissipate energy. The internal structure of a material can also be sampled using through going waves, which acquire signatures of the microstructure while propagating through and interacting with the material. We used ultrasonic probes in both passive and active modes: passive recordings allowed us to measure the energy release associated with acoustic emissions, and active pulsing was used to measure both variations of sound velocities and acoustic wave transmissivity in the samples under confining pressure. As macroscale behavior arises from microscale effects, data from all scales are needed to produce a robust picture of deformation dynamics.

This paper presents mechanical results from deformation tests followed by observations of internal structure based on acoustic emissions and ultrasonic pulsing. We show that as the LL6 chondritic material encounters higher confining pressures up to 50 MPa, the samples become stronger and stiffer and emit high-energy acoustic waves. With increasing confining pressure above 50 MPa, the material supports lower stresses, continues to stiffen, and dissipates less energy via AEs. Our observations indicate that confining pressure and associated porosity closure exert a strong control on the deformational behavior of LL6 chondrites, such that the dissipation of strain energy via brittle deformation is less pronounced at higher confining pressures.

SELTZER ET AL. 2 of 11

# 2. Methods

These tests were conducted on samples from the Kilabo meteorite, an LL6 chondrite. Icy moons are thought to have broadly chondritic silicate interiors: Néri et al. (2020) suggest that the cores of Titan and Ganymede (and possibly Callisto) are carbonaceous chondrites, while Kuskov and Kronrod (2005) infer a low metallicity and/or low iron (L/LL) composition for the interior of Europa (and, again, possibly Callisto), and Neumann and Kruse (2019) find an ordinary chondritic (OC) composition (likely L/LL) for the rocky core of Enceladus. Previous experiments suggest that strength differences between carbonaceous and ordinary chondrites are related to the higher porosity of carbonaceous chondrites rather than any inherent difference in the material composition (Flynn et al., 2018; Pohl & Britt, 2020).

The meteoritic material was impregnated in epoxy to allow sample preparation into 6.25 mm diameter cores, which were ground into right-rectangular cylinders prior to laboratory deformation. The mechanical properties of the epoxy were measured and found to influence the strength and stiffness of our material only marginally (Figure S1; see Supporting Information S1 Note 2 for further discussion of the stiffness of the meteoritic material with potential epoxy contribution removed). The samples were jacketed in soft PVC tubing and then further encased in Teflon heat shrink tubing prior to deformation (Figure S2 in Supporting Information S1). Prior to deformation, the LL6 chondritic material had ~15% microporosity, calculated via grain-level thresholding of computed tomography (CT) images, and a mean density of ~2.5 g/cm³, calculated from the measured weight and volume. However, these (and other) properties are heterogeneously distributed throughout the samples. Samples were taken from the interior of the meteorite, and there was no alteration crust present. Deformation was performed in a Paterson gas medium deformation apparatus (Paterson, 1990) housed in the Rock Mechanics Laboratory at MIT. This machine allows us to exert triaxial stress on the samples. The stress tensor is described by the three principal stress components  $(\sigma_1, \sigma_2, \sigma_3)$ , listed in descending order of compressive magnitude  $(\sigma_1 > \sigma_2 > \sigma_3)$ . A summary of the experimental parameters can be found in Table S1 in Supporting Information S1, and a setup schematic can be found in Figure S2 in Supporting Information S1.

We applied isostatic confining pressures (Pc, which here corresponds to the minimum compressive principal stress  $\sigma_3$ ) of up to 100 MPa, and deformed the samples at room temperature (296 K) and constant strain rates of  $10^{-5}$  s<sup>-1</sup>, resulting in a triaxial stress state ( $\sigma_1 > \sigma_2 = \sigma_3$ ). Differential stress ( $\sigma_1 - \sigma_3$ ) continued to increase until peak strength, the point at which the material could not support any more stress and began to weaken (Figure 3a).

Custom data acquisition system (DAQ) was used in order to record passive AEs and pass active ultrasonic pulses through the samples at regular time intervals. Custom-made miniature piezoelectric sensors with a diameter of 1.5 mm were created by cementing a piezo-element (0.5 mm tall) within a metallic tube. The piezo-element was then coated with gold to achieve high electrical conductivity. These sensors were attached to microsprings and threaded through pistons to allow constant coupling between the sensor and the sample during deformation. Brass elements of the same diameter as the sensor and 5 mm in length were attached at the pulsing side of the sensor. Signals were amplified at  $\sim$ 60 dB and recorded at 50 MS/s rate with 12 bit resolution using a digital oscilloscope (TiePie HS4-50). The majority of amplified signals fell in the frequency range of  $\sim$ 50 kHz to 2 MHz. One of the sensors was set to pulse P-waves (Y-cut LiNbO<sub>3</sub>), and the other one could receive both P- and S-waves (X-cut LiNbO<sub>3</sub>). The pulsed P-waves convert to S-waves at the interface between the sample and the brass piece of the same diameter of the pulsing-side sensor, which was placed in the sample setup in order to ensure that this wave conversion occurred. We tested and calibrated this procedure by replacing the meteorite sample with an alumina dummy with well-known and characterized P- and S-wavespeeds in an otherwise identical experimental set-up. We confirmed that the first weak arrivals correspond to P-wave velocity while the first strong motion corresponds to S-wave velocity (Figures S4 and S6 in Supporting Information S1).

Brittle deformation occurred during both pressurization and deformation, releasing strain energy and causing vibrations within the sample. The received signals were recorded as displacements at the end of the sample, representing a convolution of three main controlling parameters of wave propagation: source characteristics, the medium through which waves travel, and the sensor response. We took Fourier transforms of the displacements u at times t into corresponding frequencies  $\omega$ , such that  $u(\omega) = \sum_t u(t)e^{-i\omega t}$ , with amplitudes  $\psi_\alpha = \{u(\omega_\alpha)\}$  over frequency levels  $\alpha$ . This expansion yields modulations to the energy state with amplitudes  $C_\alpha$  and eigenvectors  $\phi_\alpha$ , which we use to characterize the state of the system  $\overrightarrow{\psi}$  such that

SELTZER ET AL. 3 of 11

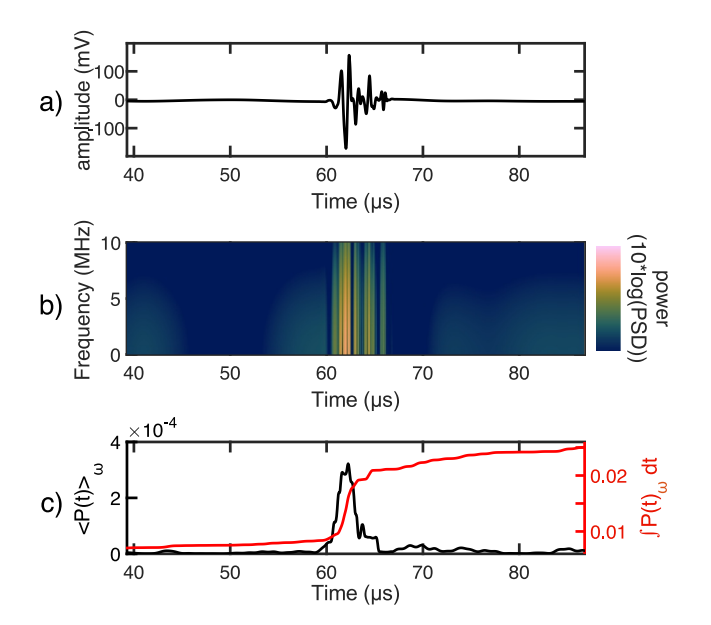


**Figure 2.** Spectral analysis of an acoustic waveform emitted during deformation under a confining pressure of 50 MPa. (a) shows the denoised acoustic waveform, (b) shows the frequency-power spectrum, colored by power as a function of power spectral density (PSD), and (c) shows power released over waveform recording time (black) and total power released (red).

$$\overrightarrow{\psi}(t) = \sum_{\alpha} C_{\alpha} e^{-i\omega_{\alpha}t} \overrightarrow{\phi}_{\alpha}. \tag{1}$$

For each acoustic emission, we smoothed over the raw emitted waveform with a window of five count intervals (0.1  $\mu$ s), and denoised it using wavelet decomposition (Figure 2a). From these data, we computed a spectrogram using the Bartlett window function W and time index  $t_i$  to yield power P, such that

$$P(t_i,\omega) = \sum_{t} W(t - t_i) \psi(t) e^{-i\omega t}.$$
 (2)

We integrated over the duration and frequency range of each event to compute the total power (Figures 2b and 2c), then normalized it by the mean power of background noise during each test. The power is a direct indication of how much energy was dissipated due to AEs. We present this quantity as a scalar value relative to the noise threshold, and discarded any events with a power-to-noise ratio below 1.5.

See Figure S3 in Supporting Information S1 for more details on acoustic emission data calibration. A comprehensive proof of this integration can also be found in the discussion of the P-parameter by Ghaffari et al. (2021).

After deformation, entire samples were imaged with the table-top microcomputed tomography (micro-CT) Skyscan system at Woods Hole Oceanographic Institution, using 5-hr scan times at a 4  $\mu$ m voxel size under 100 kV acceleration voltage.

# 3. Results

# 3.1. Mechanical Data

The peak strength of the samples generally increased with confining pressure (Pc) before reaching a maximum between 40 and 50 MPa Pc (Figure 3a). Above ~50 MPa confining pressure, peak strength decreased with increasing confining pressure. Notably, no test was able to sustain maximum axial principal compressive stresses ( $\sigma_1$ ) greater than ~360 MPa (Figure 3b); the three strongest tests all failed near this bound, within 2 MPa of axial stress of one another. Increases in confining pressure above 50 MPa therefore led to decreases in differential stress (Figure 3c). In all cases, the strain at peak strength at the point of failure remained close to 3%.

The failure envelopes of the experimentally deformed samples are represented as Mohr circles in Figure 3c. These Mohr circles are a graphical representation of the stress state within a rock at the point of failure, plotted in normal stress ( $\sigma_n$ ) versus shear stress ( $\tau$ ) space such that

$$\sigma_n = \frac{\sigma_1 + \sigma_3}{2} + \frac{\sigma_1 - \sigma_3}{2} \cos 2\theta; \ \tau = \frac{\sigma_1 - \sigma_3}{2} \sin 2\theta, \tag{3}$$

where  $\theta$  is the orientation of the normal to the fault plane with respect to  $\sigma_1$ . The Mohr-Coulomb failure envelope tangent to the circles indicates the stress conditions expected at failure:

$$\tau = 0.8\sigma_n + 28,\tag{4}$$

in units of MPa.

This linear failure envelope is valid only for samples deformed below  $\sim$ 50 MPa Pc. Byerlee's rule, which states that the shear stress needed to slide rocks along a pre-existing fault surface, is defined by

$$\tau = 0.85 \,\sigma_n, \qquad \sigma_n < 200 \,\text{MPa},$$
  

$$\tau = 0.6 \,\sigma_n + 0.5, \qquad \sigma_n \ge 200 \,\text{MPa}$$
(5)

SELTZER ET AL. 4 of 11

, Wiley Online Library on [08/07/2024]. See the Terms and Conditions

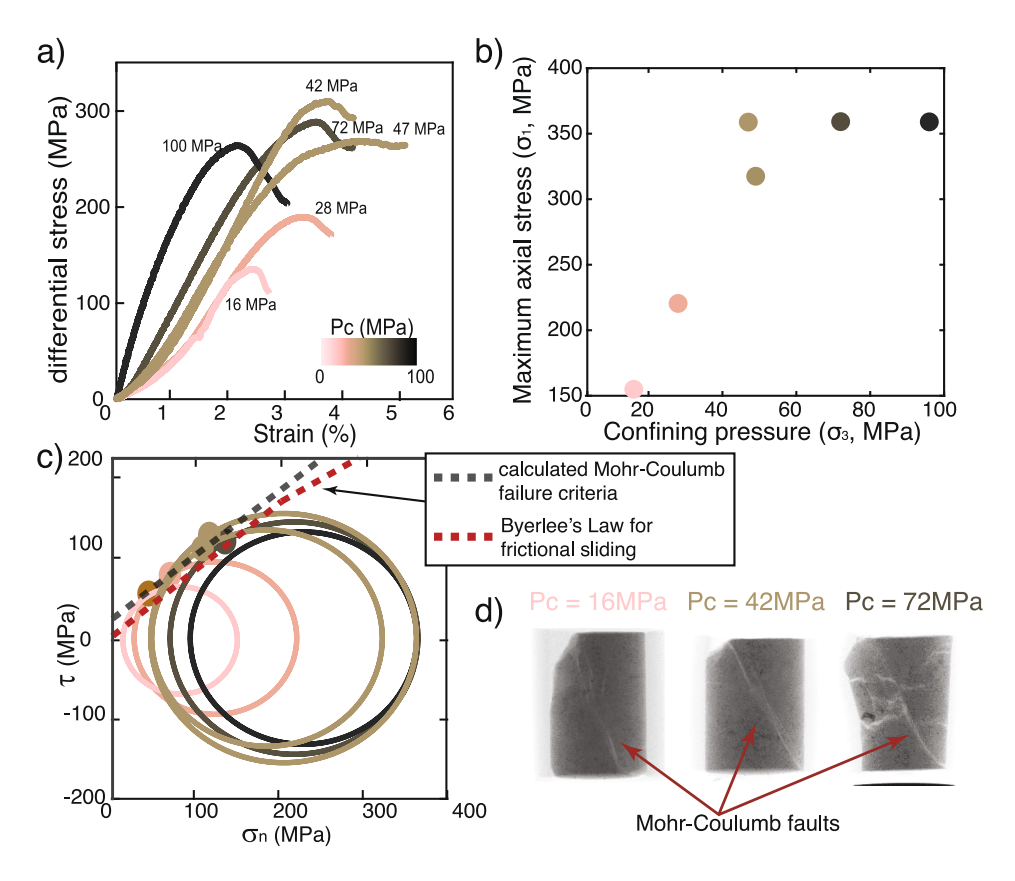


**Figure 3.** Mechanical results from deformation tests, represented as (a) stress/strain curves, colored by confining pressure (Pc), also labeled on individual curves, (b) Maximum axial compressive stress reached during each test, colored by confining pressure, (c) Mohr circles, plotted in shear stress versus normal stress  $(\tau, \sigma_n)$  space, with a tangent line indicating the Mohr-Coulomb failure envelope and large dots representing fault orientation developed at failure, as well as a line showing Byerlee's Law for frictional sliding, and (d) CT images of deformed samples, with final faults indicated.

(Byerlee, 1978). Byerlee's rule falls below the range of stress states recorded during deformation tests, as expected for the deformation of intact rocks.

During several tests of up to 50 MPa confining pressure, we monitored sound velocities using the piezoelectric sensors placed above and below the sample (see Table S1 in Supporting Information S1). From these measurements, we characterized dynamic (unrelaxed) Young's moduli via seismic wavespeeds for P- and S-waves  $(V_P, V_S, P_S, P_S)$ , respectively),

$$E_{\rm dyn} = \frac{\rho V_s^2 (3V_P^2 - 4V_S^2)}{V_P^2 - V_S^2}.$$
 (6)

We compared the unrelaxed, microscale  $E_{\rm dyn}$  with the observed macroscale Young's modulus derived from mechanical data on differential stress,  $\sigma$ , and strain,  $\varepsilon$ , such that

$$E_{\rm qs} = \frac{\sigma}{\epsilon}.\tag{7}$$

The Young's modulus, which relates stress to axial strain, describes a material's stiffness. For perfectly elastic materials, elastic deformation is by definition time-independent and reversible and so no strain-rate dependence of moduli is expected. Natural materials, however, are typically stiffer at higher frequencies, indicating the

SELTZER ET AL. 5 of 11

, Wiley Online Library on [08/07/2024]. See the Terms and Conditions (https://onlinelibrary.wiley.

conditions) on Wiley Online Library for rules of use; OA articles are governed by the applicable Creat

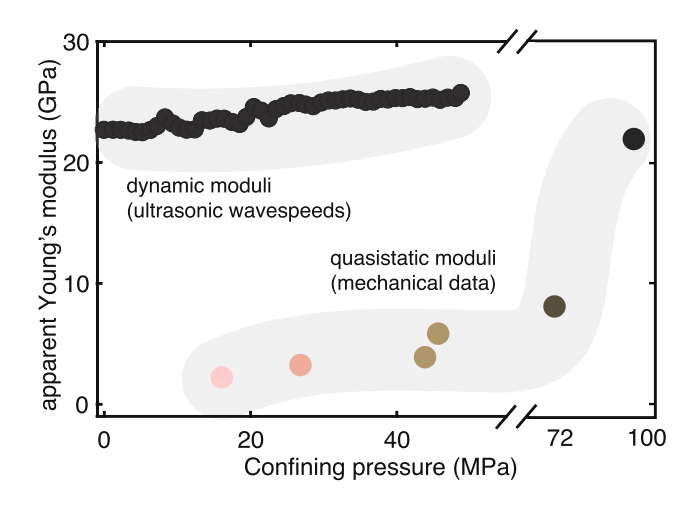


**Figure 4.** Observed quasistatic Young's modulus for each test from bulk deformation calculated using Equation 7 (large dots, colored by confining pressure) and dynamic Young's modulus from ultrasonic probing calculated using Equation 6 (small black dots). All are plotted as a function of confining pressure, with each deformation test colored and plotted by its confining pressure. See Figure S1 in Supporting Information S1 for potential effects of epoxy on these measurements.

presence of a viscous element contributing to measured mechanical responses (Davarpanah et al., 2020; Jackson, 2015; Kolesnikov, 2009; van Heerden, 1987). In the ultrasonic pulsing experiments used to calculate the dynamic modulus, waves are generated in the hundreds of kHz range and so there is little time for stress relaxation. The calculated unrelaxed Young's modulus is therefore higher during dynamic probing than during longer-timescale, quasistatic bulk deformation sampled at Hz frequencies (Figure 4).

#### 3.2. Ultrasonic Probes

#### 3.2.1. Acoustic Emissions

All samples released energy via brittle deformation processes, both during isotropic pressurization and sample-scale triaxial deformation. Acoustic emissions occurred at all sampled pressures (Figures 5a and 5d), and were most powerful at low confining pressures (<25 MPa Pc) and around the confining pressures corresponding to peak material strength (~50 MPa Pc) (Figure 5d). The integrated power and maximum amplitudes of each AE decreased slightly with increasing differential stress ( $\sigma_1$ – $\sigma_3$ ) (Figures 5b and 5e), and the power-to-noise ratio was largest for low values of  $\sigma_1$  (Figures 5c and 5f). Many of these dissipative events occurred during the nominally "elastic" deformation period, when differential stress is low and no energy release is expected. The material also emitted energy through AEs during isotropic pressurization cycles (Figure 6d) when differential stress is nominally zero.

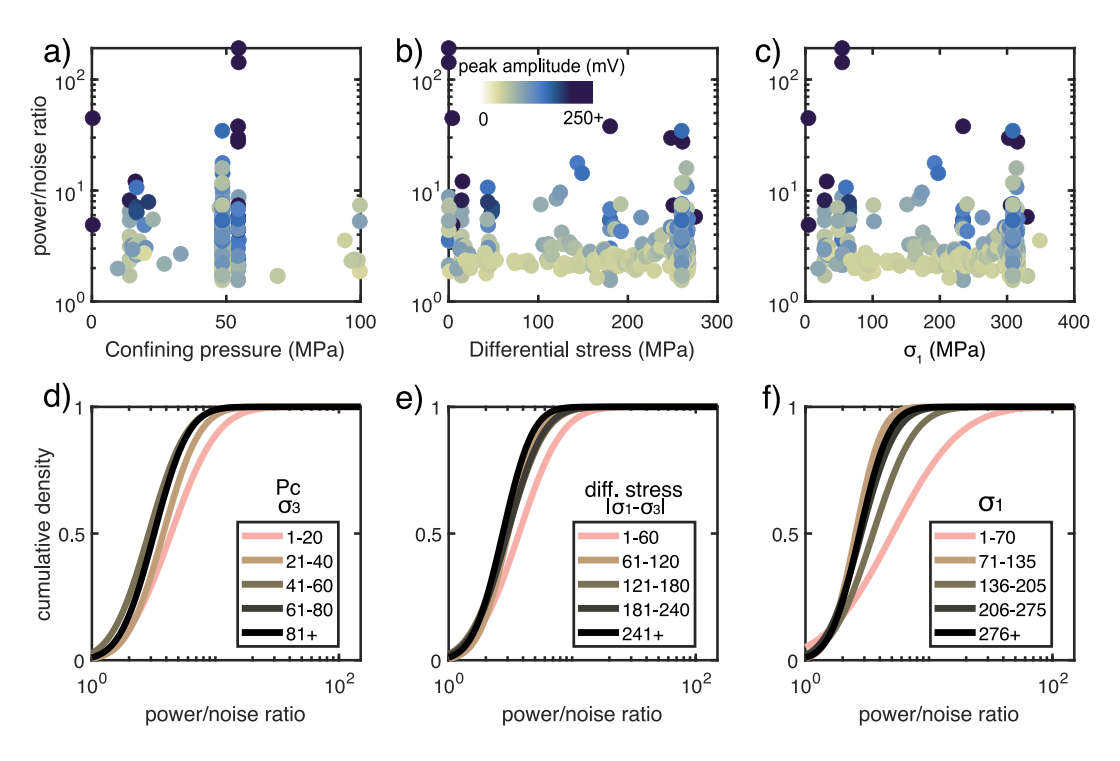


Figure 5. (a–c) Power of AEs, normalized by noise threshold for each test, as a function of (a) confining pressure (Pc),  $\sigma_3$ , (b) differential stress  $(\sigma_1 - \sigma_3)$ , (c) axial stress,  $\sigma_1$ . Each point represents one AE event, and is colored by the maximum amplitude of that event following the colorbar in panel (b). (d–f) Lognormal cumulative distribution functions of total power per event, evolving as a function of (d) confining pressure (Pc),  $\sigma_3$ , (e) differential stress  $(\sigma_1 - \sigma_3)$ , and (f) axial stress,  $\sigma_1$ . Colored lines correspond to specific stress ranges in MPa, which are defined specifically for each panel in its interior legend.

SELTZER ET AL. 6 of 11

2169/100, 2024, 7, Downloaded from https://aguputs.omlinelibrary.wiley.com/doi/10.1029/2024/E008296 by Maeje Pe. - Massachuserts Institute of Technolo , Wiley Online Library on [08/07/2024]. See the Terms and Conditions (https://onlinelibrary.wiley.com/ebms-and-conditions) on Wiley Online

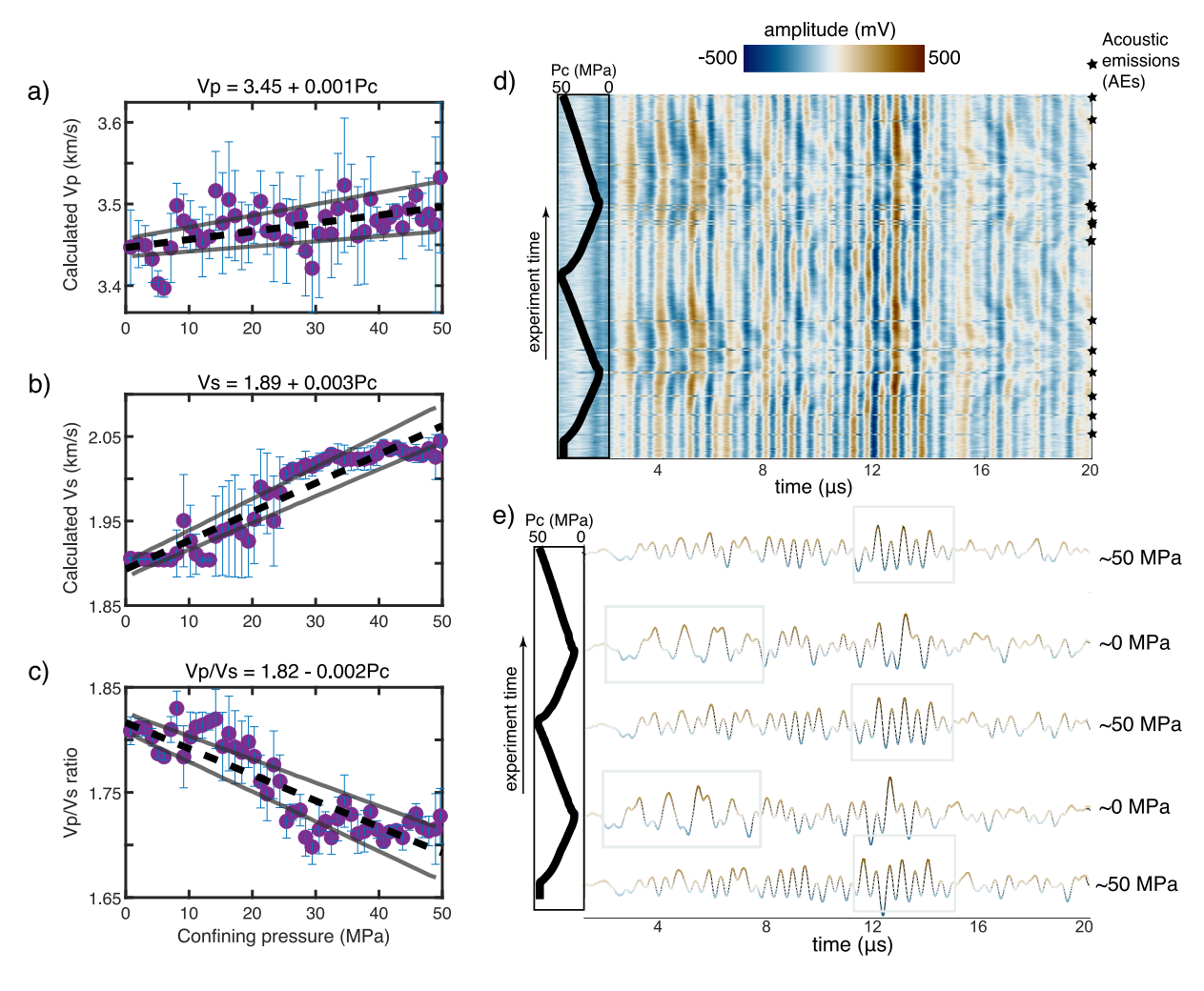


Figure 6. Results from ultrasonic pulsing during confining pressure oscillation. (a) P-wavespeeds (Vp). (b) S-wavespeeds (Vs). (c) Vp/Vs ratio. For (a-c), linear trendlines as a function of confining pressure are shown in black, per equations in the format  $V = V_0 + mPc$ , where V and  $V_0$  have the same units  $(km s^{-1} \text{ for } Vp \text{ and } Vs, \text{ and unitless for } Vp/Vs)$ , m has units of  $km s^{-1} MPa^{-1}$  for Vp and Vs, and  $MPa^{-1}$  for Vp/Vs, and Pc has units of MPa, with gray lines denoting 90% confidence interval. (d) Two full depressurization-repressurization cycles and resultant waveforms. Black line indicates pressure conditions. Waveforms are plotted as a vertical function of increasing experimental time, and color corresponds with normalized amplitude, from blue (high negative amplitude) to brown (high positive amplitude), per colorbar. Horizontal, discontinuous lines marked with stars are energetic acoustic emission events, which are separate from the pulsed ultrasonic waves shown here. (e) Sample waveforms from 0 to 50 MPa confining pressure at each maximum or minimum in the cycle. Similar parts of the waveform at 0 and 50 MPa are highlighted in light gray boxes.

# 3.2.2. Ultrasonic Pulsing

To determine wavespeeds as a function of pressure, we sent ultrasonic pulses through a sample while cycling confining pressure between 0 and 50 MPa (Figures 6a–6c). This procedure also allowed us to examine whether pressure oscillations changed the internal structure of our material and validate our results by collecting this velocity data over several pressurization-depressurization cycles. Waveforms and arrival time picking are detailed in Figure S4 in Supporting Information S1; modeled formation of S-waves in our experimental setup is detailed in Figure S5 in Supporting Information S1, and calibrations on homogeneous alumina rods using the same sensors are detailed in Figure S6 in Supporting Information S1. We examined the entire waveform to determine how the structure affects throughgoing waves (Figures 6d and 6e). The first arrival of a waveform at the sensor location represents the shortest path between the source and receiver, while the coda of these waveforms, which represent multiple "echoes" as the waveforms bounce around the sample, travel for a longer distance in the medium and are therefore sensitive to changes in the internal structure of the rock. The amplitudes and arrival times of throughgoing waves changed with confining pressure conditions, such that at lower pressures, comparable parts of the waveform arrived later, and at higher pressures, they arrived earlier (Figure 6d), suggesting

SELTZER ET AL. 7 of 11

that the modifications to internal structure of the material occur on smaller length scales than sampled by ultrasonic waves and therefore may not be visible to ultrasonic waves, regardless of recent pressure history.

#### 4. Discussion

We observed that with increasing confining pressure of up to 50 MPa, the LL6 chondritic material showed an increase in peak strength, increase in Young's modulus, and increase in ultrasonic velocities. As confining pressures increased above 50 MPa, the LL6 chondritic material studied showed a decrease in peak strength but a further increase in Young's modulus. The material also dissipates energy through acoustic emissions even at very low differential stress values. These results suggest that the mechanical and acoustic properties of chondritic material, and therefore possibly the cores of icy moons, are dependent on confining pressure and differential stress.

#### 4.1. Discussion of Mechanical Data

The stony LL6 chondritic material studied here initially strengthens with increasing confining pressure and then undergoes a drop in peak differential stress above confining pressures >50 MPa (Figures 3a and 3c). This observed behavior is similar to the "cap model" for compaction and deformation of porous Earth materials. In the cap model, porosity decreases steadily with increasing pressure as the load-bearing matrix rock is compressed elastically, before dropping rapidly at a point of pore compaction (P\*) for isotropic stresses, when the strength of the rock matrix is overcome and pore collapse occurs throughout the rock volume. If stress is anisotropic, this drop occurs at a point of compactive yield stress (C\*), where the load-bearing framework undergoes a shear-induced collapse. At stresses higher than C\*, cataclastic flow takes over as the primary mode of deformation (Wong & Baud, 2012).

Pore closure may therefore proceed in a predictable yet discontinuous manner across icy moon environments. When differential stress is present, porosity should decrease somewhat steadily with increasing confining pressure; at a confining pressure corresponding to P\*, this porosity should suddenly drop. It is possible that the maximum principal compressive stress seen in our tests, 360 MPa (Figure 3b), also represents the condition for total pore closure via shear-enhanced compaction. This value matches closely with *total* pore closure conditions near 350 MPa assumed in models such as Planet Profile (Styczinski et al., 2023; Vance et al., 2018); these models may then predict the point of total pore closure but predict it using a continuous slow closure rather than a sudden large degree of pore closure at specific compaction points.

Given that the peak strengths of the LL6 chondritic material are tens to hundreds of MPa (Figure 2a), at least an order of magnitude higher than predicted stresses within rocky cores (Gao & Stevenson, 2013; McKinnon, 2013), we assume that material in the rocky cores will likely not approach its peak strength, and that most to all deformation therefore occurs in small-strain, nominally elastic regimes. The elastic stiffness applicable to this regime increases at >50 MPa confining pressure (Figure 4), indicating that, given the same magnitude of stress, chondritic material under higher confining pressure will achieve smaller magnitudes of strain than chondritic material under lower confining pressure. The mechanisms of deformation may then be different in larger moons than in smaller moons, due to the increased confining pressures from increased overburden at the rock-ocean or rock-ice interface. In bodies where rocky interiors are under higher confining pressures, material may have a higher Young's modulus and thus require higher stresses to deform significantly; in lower-pressure environments, material may be more compliant and thus deform more easily.

Viscoelastic deformation of silicate interiors has been suggested as a mechanism for heat generation and tidal dissipation in Enceladus and Europa (Kang et al., 2020; Liao et al., 2020; Rovira-Navarro et al., 2022), but the mechanisms responsible for viscous response in a cold chondritic layer have not yet been identified. Silicates typically require elevated pressures and temperatures for viscous deformation (e.g., Kohlstedt & Hansen, 2015). Brittle creep, a mechanism that is active in silicate rocks at low pressures and temperatures (Bernabé & Peč, 2022; Brantut et al., 2013), may generate an additional apparent viscous response, contributing to the total heat dissipation via brittle deformation processes such as microcracking and frictional sliding along the generated crack surfaces. Similar effects may arise from pore closure and reopening. While not truly a viscous response, the presence of brittle creep could serve as a nonlinear viscous element over short timescales and thus should be considered in models for viscoelastic core deformation. The decrease in Young's modulus with decreasing

SELTZER ET AL. 8 of 11

sampling frequency (Figure 4) further suggests possible apparent viscous dissipation of energy, as the material is less stiff over longer timescales and therefore relaxes significantly.

#### 4.2. Discussion of Acoustic and Ultrasonic Data

Dissipative acoustic emissions from brittle deformation events occurred at all pressures sampled, even at low differential stresses, indicating that even small changes to local stresses can initiate cracks (Figure 4). The ratio between P- and S-wavespeeds also decreased with increasing confining pressure (Figure 5c), which occurs as damage increases (Wang et al., 2012). We suggest that brittle failures such as microcracking and associated frictional sliding on cracks and faults could be continuously occurring in the rocky interiors of icy satellites, where deviatoric stresses can be on the order of 1 MPa or higher, changing periodically with the orbit of the satellite (Gao & Stevenson, 2013; McKinnon, 2013). As these acoustic emission events occurred during the nominally elastic component of deformation (low differential stress, low strain; Figures 5b and 5e), we suggest that the energy from microscale brittle mechanisms could be associated with the apparent viscous response necessary for dissipation in the silicate core. This observation, in conjunction with changes to stiffness described in the previous subsection, further suggests that moons with thinner, less massive hydrospheres could receive proportionally more heat over their lifetimes from the deformation of their rocky interiors than larger moons, as their cores will be more deformable at low pressures and therefore able to dissipate heat during viscoelastic deformation. Local values of differential stress as well as the maximum principal compressive stress ( $\sigma_1$ ) will likely be lower in smaller moons as well, corresponding to the most energetic brittle deformation events seen in our tests (Figures 5c and 5f).

Brittle deformation and frictional sliding during deformation can release heat and generate new surface area. Modeling by Rovira-Navarro et al. (2022) found that rock-water interaction (via increasing permeability) increases dissipation throughout a porous core. Fresh surface area would encourage serpentinization, which has been suggested as a mechanism for generating hydrogen within the oceans of icy bodies (Kamata et al., 2019; McCollom et al., 2022; Neveu et al., 2015; Vance & Melwani Daswani, 2020) or cultivation of organic materials which have risen to Titan's surface (Castillo-Rogez & Lunine, 2010). Many of these reactions include volume increase, which modifies the local stress field, encouraging further cracking within the silicate body. One excellent opportunity for future laboratory studies is the measurement of the acoustic properties of aqueously altered chondritic material, which should exist at the rock-ocean boundary.

The current data set is insufficient to constrain the expected magnitude of potential heating effects. In order to properly constrain the amount of heat that could be released through brittle deformation mechanisms at elevated confining pressures and low differential stresses, dedicated experiments aimed at measuring the viscoelastic properties of confined rocky chondritic material under oscillatory loading are needed. These experiments presented here were conducted under dry conditions, but as pore fluids change the local stress state by lowering the effective pressure, materials at the ocean-silicate interface could potentially dissipate more energy than we observed in the lab. Additionally, while our deformation experiments are conducted at relatively slow strain rates, they are not identical to the timescales and frequencies of tidal deformation. Under realistic tidal forcing periods, the strength of porous rocks is expected to be low (Bagde & Petroš, 2009; Peng et al., 2020), further increasing the likelihood of brittle deformation in response to small stress changes. In order to identify the magnitude of a possible viscous element contributing to deformation in chondritic material over additional frequencies and pressure ranges, future experiments studying the mechanical and acoustic responses of pressurized chondritic material to forced oscillatory loading are needed.

# 5. Conclusions

We characterized the mechanical properties of stony LL6 chondritic material under a range of confining pressures by defining a failure envelope, measuring ultrasonic wavespeeds, and retrieving both static and dynamic elastic moduli. The mechanical results suggest that the porosity of the deforming chondritic material decreases significantly at a confining pressure of  $\sim 50$  MPa, reducing the peak strength and increasing the Young's modulus of the rocky chondritic material. We also observed energy release arising from small changes in stress. Brittle deformation may thus represent an apparent viscous response which enhances heat dissipation within rocky cores and mantles. Furthermore, the energy release associated with brittle deformation processes also occurrs during nominally isotropic states of pressurization and depressurization.

SELTZER ET AL. 9 of 11

com/doi/10.1029/2024JE008296 by Matej

CS received support from the

Massachusetts Space Grant Consortium

Science Fellowship, Figures were plotted

using perceptually uniform colormaps

from Crameri (2021). CORD laboratory

technician support by NSF Grant 2054414

is gratefully acknowledged; thank you to

Uli Mok for assistance with prep and

deformation experiments. Thank you to

Veronique LeRoux for CT scans, Mark

Panning, Mohit Melwani Deswani, and

on the project. This work benefited

anonymous reviewers.

Laurent Pou for discussions on icy moon

interiors, and to Rick Binzel for early input

significantly from the suggestions of two

and the MathWorks MIT School of

Pressure, and the resultant amount of porosity that a material can maintain, may therefore be a strong control on the dissipative potential of silicate interiors: the silicate interiors of larger, higher-pressure icy moons may be relatively dense, stiff, and impermeable, suggesting that rocky interiors of larger moons could be less deformable than those of smaller moons, and therefore dissipate proportionally less energy in response to tidal forcing. We also see that the release of energy persists as deformation continues, suggesting that dissipation through rocky deformation can occur at many points in diurnal tidal forcing cycles. However, further experimental measurements are needed to constrain the potential magnitude of this effect.

# **Data Availability Statement**

All mechanical, ultrasonic, and acoustic data can be found at Seltzer (2023).

# Acknowledgments References

Aygün, B., & Čadek, O. (2022). A new approach to modeling the tidal dissipation in subsurface oceans of icy moons of Jupiter and Saturn (other). Oral. https://doi.org/10.5194/epsc2022-968

Bagde, M. N., & Petroš, V. (2009). Fatigue and dynamic energy behaviour of rock subjected to cyclical loading. *International Journal of Rock Mechanics and Mining Sciences*, 46(1), 200–209. https://doi.org/10.1016/j.ijrmms.2008.05.002

Bernabé, Y., & Peč, M. (2022). Brittle creep and failure: A reformulation of the wing crack model. *Journal of Geophysical Research: Solid Earth*, 127(9), e2022JB024610. https://doi.org/10.1029/2022JB024610

Brantut, N., Heap, M. J., Meredith, P. G., & Baud, P. (2013). Time-dependent cracking and brittle creep in crustal rocks: A review. *Journal of Structural Geology*, 52, 17–43. https://doi.org/10.1016/j.jsg.2013.03.007

Byerlee, J. (1978). Friction of rocks 116.

Castillo-Rogez, J. C., & Lunine, J. I. (2010). Evolution of Titan's rocky core constrained by Cassini observations. *Geophysical Research Letters*, 37(20). https://doi.org/10.1029/2010GL044398

Crameri, F. (2021). Scientific colour maps. https://doi.org/10.5281/zenodo.5501399

Davarpanah, S. M., Ván, P., & Vásárhelyi, B. (2020). Investigation of the relationship between dynamic and static deformation moduli of rocks. The journal Geomechanics and Geophysics for Geo-Energy and Geo-Resources, 6(1), 29. https://doi.org/10.1007/s40948-020-00155-z.

Eitzen, D. G., & Wadley, H. N. G. (1984). Acoustic emission: Establishing the fundamentals. The Journal of Research of the National Institute of Standards and Technology, 89(1), 75. https://doi.org/10.6028/jres.089.008

Flynn, G. J., Consolmagno, G. J., Brown, P., & Macke, R. J. (2018). Physical properties of the stone meteorites: Implications for the properties of their parent bodies. *Geochemistry*, 78(3), 269–298. https://doi.org/10.1016/j.chemer.2017.04.002

Gao, P., & Stevenson, D. J. (2013). Nonhydrostatic effects and the determination of icy satellites' moment of inertia. *Icarus*, 226(2), 1185–1191. https://doi.org/10.1016/j.icarus.2013.07.034

https://doi.org/10.1010/j.icarus.2015.07.034
Ghaffari, H. O., Mok, U., & Pec, M. (2021). On calibration of piezoelectric sensors with laser doppler vibrometer. *Journal of the Acoustical Society of America*, 150(4), 2503–2513. https://doi.org/10.1121/10.0006445

Ghaffari, H. O., Nasseri, M. H. B., & Young, R. P. (2014). Faulting of rocks in a three-Dimensional stress field by micro-anticracks. *Scientific Reports*, 4(1), 5011. https://doi.org/10.1038/srep05011

Hogan, J. D., Kimberley, J., Hazeli, K., Plescia, J., & Ramesh, K. T. (2015). Dynamic behavior of an ordinary chondrite: The effects of microstructure on strength, failure and fragmentation. *Icarus*, 260, 308–319. https://doi.org/10.1016/j.icarus.2015.07.027

Jackson, I. (2015). Properties of rocks and minerals: Physical origins of anelasticity and attenuation in rock. In Treatise on Geophysics (pp. 539–571). Elsevier. https://doi.org/10.1016/B978-0-444-53802-4.00045-2

Kamata, S., Nimmo, F., Sekine, Y., Kuramoto, K., Noguchi, N., Kimura, J., & Tani, A. (2019). Pluto's ocean is capped and insulated by gas hydrates. *Nature Geoscience*, 12(6), 407–410. https://doi.org/10.1038/s41561-019-0369-8

Kang, W., Bire, S., Campin, J.-M., Sotin, C., German, C., Thurnherr, A., & Marshall, J. (2020). Differing Enceladean ocean circulation and ice shell geometries driven by tidal heating in the ice versus the core.

Kimberley, J., & Ramesh, K. T. (2011). The dynamic strength of an ordinary chondrite. *Meteoritics & Planetary Sciences*, 46(11), 1653–1669. https://doi.org/10.1111/j.1945-5100.2011.01254.x

Kohlstedt, D. L., & Hansen, L. N. (2015). Constitutive equations, rheological behavior, and viscosity of rocks. In *Treatise on Geophysics* (pp. 441–472). Elsevier. https://doi.org/10.1016/B978-0-444-53802-4.00042-7

Kolesnikov, Y. I. (2009). Dispersion effect of velocities on the evaluation of material elasticity. *Journal of Mining Science*, 45(4), 347–354. https://doi.org/10.1007/s10913-009-0043-4

Kuskov, O. L., & Kronrod, V. A. (2005). Internal structure of Europa and Callisto. *Icarus*, 177(2), 550–569. https://doi.org/10.1016/j.icarus.2005.04.014

Lei, X., & Ma, S. (2014). Laboratory acoustic emission study for earthquake generation process. Earthquake Science, 27(6), 627–646. https://doi.org/10.1007/s11589-014-0103-y

Li, X., Si, G., Oh, J., Canbulat, I., Xiang, Z., & Zhang, X. (2021). Laboratory characterisation of anisotropic and heterogeneous damage of rock sample using acoustic emission and ultrasonic monitoring technologies. *IOP Conference Series: Earth and Environmental Science*, 861(2), 022040. https://doi.org/10.1088/1755-1315/861/2/022040

Liao, Y., Nimmo, F., & Neufeld, J. A. (2020). Heat production and tidally driven fluid flow in the permeable core of Enceladus. *Journal of Geophysical Research: Planets*, 125(9), e2019JE006209. https://doi.org/10.1029/2019JE006209

Mair, K., Elphick, S., & Main, I. (2002). Influence of confining pressure on the mechanical and structural evolution of laboratory deformation bands. *Geophysical Research Letters*, 29(10), 49-1–49-4. https://doi.org/10.1029/2001GL013964

McCollom, T. M., Klein, F., & Ramba, M. (2022). Hydrogen generation from serpentinization of iron-rich olivine on Mars, icy moons, and other planetary bodies. *Icarus*, 372, 114754. https://doi.org/10.1016/j.icarus.2021.114754

McKinnon, W. B. (2013). The shape of Enceladus as explained by an irregular core: Implications for gravity, libration, and survival of its subsurface ocean. *Journal of Geophysical Research: Planets*, 118(9), 1775–1788. https://doi.org/10.1002/jgre.20122

SELTZER ET AL. 10 of 11



# Journal of Geophysical Research: Planets

- 10.1029/2024JE008296
- Mulliken, A. D., & Boyce, M. C. (2006). Mechanics of the rate-dependent elastic-plastic deformation of glassy polymers from low to high strain rates. *International Journal of Solids and Structures*, 43(5), 1331–1356. https://doi.org/10.1016/j.ijsolstr.2005.04.016
- Néri, A., Guyot, F., Reynard, B., & Sotin, C. (2020). A carbonaceous chondrite and cometary origin for icy moons of Jupiter and Saturn. Earth and Planetary Science Letters, 530, 115920. https://doi.org/10.1016/j.epsl.2019.115920
- Neumann, W., & Kruse, A. (2019). Differentiation of Enceladus and retention of a porous core. *The Astrophysical Journal*, 882(1), 47. https://doi.org/10.3847/1538-4357/ab2fcf
- Neveu, M., Desch, S. J., & Castillo-Rogez, J. C. (2015). Core cracking and hydrothermal circulation can profoundly affect Ceres' geophysical evolution. *Journal of Geophysical Research: Planets*, 120(2), 123–154. https://doi.org/10.1002/2014JE004714
- Nimmo, F., & Pappalardo, R. T. (2016). Ocean worlds in the outer solar system. *Journal of Geophysical Research: Planets*, 121(8), 1378–1399. https://doi.org/10.1002/2016JE005081
- O'Ghaffari, H., Peč, M., Mittal, T., Mok, U., Chang, H., & Evans, B. (2023). Microscopic defect dynamics during a brittle-to-ductile transition. Proceedings of the National Academy of Sciences of the United States of America, 120(42), e2305667120. https://doi.org/10.1073/pnas. 2305667120
- Paterson, M. S. (1990). Rock deformation experimentation. In *The brittle-ductile transition in rocks* (pp. 187–194). American Geophysical Union (AGU). https://doi.org/10.1029/GM056p0187
- Peng, K., Zhou, J., Zou, Q., & Song, X. (2020). Effect of loading frequency on the deformation behaviours of sandstones subjected to cyclic loads and its underlying mechanism. *International Journal of Fatigue*, 131, 105349. https://doi.org/10.1016/j.ijfatigue.2019.105349
- Pohl, L., & Britt, D. T. (2020). Strengths of meteorites—An overview and analysis of available data. *Meteoritics & Planetary Sciences*, 55(4), 962–987. https://doi.org/10.1111/maps.13449
- Ramesh, K. T., Stickle, A. M., & Kimberley, J. (2017). Rocks, shocks and asteroids, and some interesting research directions in Mechanics: 2015 Murray Lecture paper. Experimental Mechanics, 57(8), 1149–1159. https://doi.org/10.1007/s11340-017-0324-9
- Rovira-Navarro, M., Katz, R. F., Liao, Y., van der Wal, W., & Nimmo, F. (2022). The tides of Enceladus' porous core. *Journal of Geophysical Research: Planets*, 127(5), e2021JE007117. https://doi.org/10.1029/2021JE007117
- Seltzer, C. (2023). Supporting data for "Mechanical properties of the rocky interiors of icy moons" [Dataset]. Zenodo. https://doi.org/10.5281/
- Styczinski, M. J., Vance, S. D., & Melwani Daswani, M. (2023). PlanetProfile: Self-consistent interior structure modeling for ocean worlds and rocky dwarf planets in Python. Earth and Space Science, 10(8), e2022EA002748. https://doi.org/10.1029/2022EA002748
- Tobie, G., Mocquet, A., & Sotin, C. (2005). Tidal dissipation within large icy satellites: Applications to Europa and Titan. *Icarus*, 177(2), 534–549. https://doi.org/10.1016/j.icarus.2005.04.006
- Vance, S. D., & Melwani Daswani, M. (2020). Serpentinite and the search for life beyond Earth. *Philosophical Transactions of the Royal Society*
- A: Mathematical, Physical & Engineering Sciences, 378(2165), 20180421. https://doi.org/10.1098/rsta.2018.0421
  Vance, S. D., Panning, M. P., Stähler, S., Cammarano, F., Bills, B. G., Tobie, G., et al. (2018). Geophysical investigations of habitability in ice-
- covered ocean worlds. Journal of Geophysical Research: Planets, 123(1), 180–205. https://doi.org/10.1002/2017JE005341 van Heerden, W. L. (1987). General relations between static and dynamic moduli of rocks. International Journal of Rock Mechanics and Mining
- Sciences and Geomechanics Abstracts, 24(6), 381–385. https://doi.org/10.1016/0148-9062(87)92262-5

  Voropaev, S. A., Kocherov, A. V., Lorenz, C. A., Korochantsev, A. V., Dushenko, N. V., Kuzina, D. M., et al. (2017). Features in constructing a certificate of strength of extraterrestrial material by the example of the Chelyabinsk meteorite. Doklady Physics, 62(10), 486–489. https://doi.org/10.1134/S1028335817100111
- Voropaev, S. A., Nugmanov, I. I., Dushenko, N. V., & Jianguo, Y. (2020). Dependence of the elastic properties of H5-chondrites (NWA 12370) on pressure. Doklady Physics, 65(11), 383–386. https://doi.org/10.1134/S1028335820110105
- Wang, X.-Q., Schubnel, A., Fortin, J., David, E. C., Guéguen, Y., & Ge, H.-K. (2012). High Vp/Vs ratio: Saturated cracks or anisotropy effects? Geophysical Research Letters, 39(11). https://doi.org/10.1029/2012GL051742
- Wong, T., & Baud, P. (2012). The brittle-ductile transition in porous rock: A review. Journal of Structural Geology, 44, 25–53. https://doi.org/10.1016/j.jsg.2012.07.010

SELTZER ET AL. 11 of 11